RAA 2020 Vol. **20** No. **4**, 45(12pp) doi: 10.1088/1674–4527/20/4/45

http://www.raa-journal.org *http://iopscience.iop.org/raa*

***R**esearch in*
***A**stronomy and*
***A**strophysics*

Spectro-polarimetric observations at the NVST: I. instrumental polarization calibration and primary measurements

Jun-Feng Hou[1], Zhi Xu[2⋆], Shu Yuan[2], Yu-Chao Chen[2], Jian-Guo Peng[2], Dong-Guang Wang[1], Jun Xu[2], Yuan-Yong Deng[1], Zhen-Yu Jin[2], Kai-Fan Ji[2] and Zhong Liu[2]

[1] National Astronomical Observatories, Chinese Academy of Sciences, Beijing 100101, China; *xuzhi@ynao.ac.cn*
[2] Yunnan Observatories, Chinese Academy of Sciences, Kunming 650216, China

Received 2019 September 6; accepted 2019 November 10

Abstract This paper is devoted to the primary spectro-polarimetric observation performed at the New Vacuum Solar Telescope (NVST) of China since 2017, and our aim is to precisely evaluate the real polarimetric accuracy and sensitivity of this polarimetry by using full Stokes spectro-polarimetric observations of the photospheric line Fe I 532.4 nm. In the work, we briefly describe the salient characteristic of the NVST as a polarimeter in terms of technology and then characterize its instrumental polarization based on the operation in 2017 and 2019. It is verified that the calibration method utilizing the instrumental polarization calibration unit (ICU) is stable and credible. The calibration accuracy can reach up to 3×10^{-3}. Based on the scientific observation of NOAA Active Region 12645 on 2017 April 5, we estimate that the residual cross-talk from Stokes I to Stokes Q, U and V, after the instrumental polarization calibration, is about 4×10^{-3} on average, which is consistent with the calibration accuracy and close to the photon noise. The polarimetric sensitivity (i.e., the detection limit) for polarized light is of the order of 10^{-3} with an integration time over 20 s. Slow modulation rate is indeed an issue for the present system. The present NVST polarimeter is expected to be integrated with a high-order adaptive optics system and a field scanner to realize 2D vector magnetic field measurements in the following instrumentation update.

Key words: techniques: polarimetric — techniques: spectroscopic — Sun: magnetic fields

1 INTRODUCTION

The 1-meter New Vacuum Solar Telescope (NVST) located at Fuxian Solar Observatory aims to observe dynamic solar structures and vector magnetic fields with high resolution (Liu et al. 2014). To achieve that, its terminals comprise a multi-channel high-resolution imaging system (Xu et al. 2014) and a high-dispersion multi-line spectrograph (Wang et al. 2013). Since 2017, the spectrograph has been improved to develop the capability of spectro-polarimetric observation. The spectro-polarimetric observation can be carried out in one or several visible spectral lines. Full Stokes profiles are all obtained, from which the vector magnetic field can be retrieved by resolving the radiative transfer for polarized radiation with an atmospheric model assumption and applying many sophisticated inversion techniques (Harvey et al. 1972; Skumanich & Lites 1987; Lagg et al. 2004).

There is a common problem that the polarimetric data measured by the polarimeter need to be calibrated for cross-talk (i.e., the linear combination) between different polarization states caused by the polarimeter itself (del Toro Iniesta 2003). It can be described as $S_{\rm obs} = X \cdot S_{\rm sun}$, where $S_{\rm sun}$ is the incident Stokes vector from the Sun to the telescope. $S_{\rm obs}$ is the direct data product from the observation. X represents the response matrix (function). The measurement accuracy of polarimetry largely depends on accurate knowledge of the matrix X. Besides many efforts to precisely build the theoretical polarization model of the entire system, since the 1980s knowledge of X could be experimentally determined with the aid of a device, which can produce incident light with a known polarization state (Baur et al. 1980). It is usually called an instrumental polarization calibration unit (ICU or PCU). This technique has been utilized by several telescopes, such as the Advanced Stokes Polarimeter at the vacuum tower telescope of National Solar Observatory (Skumanich et al. 1997), the Domeless Solar Telescope at Hida Observatory

⋆ Corresponding author

(Kiyohara et al. 2004; Anan et al. 2012; Anan et al. 2018), the German Vacuum Tower Telescope at Tenerife (Beck et al. 2005), the Solar Optical Telescope aboard *Hinode* (Ichimoto et al. 2008), the 1.5 m solar telescope GREGOR (Hofmann et al. 2012) and so on. An ICU designed by the staff at Huairou Solar Observing Station has been equipped on the NVST since 2017 (Hou et al. 2017) in order to precisely determine the matrix X.

In this work, we report the current spectro-polarimetric observation performed at the NVST and figure out the main polarization characteristic of the NVST, including the polarization modulation mode, the procedure to calibrate and remove the instrument polarization, the actual polarimetric accuracy and sensitivity, etc. These analysis are mainly based on the spectro-polarimetric observations run in 2017 and 2019. It is worth noting that both the present observation and analysis are preliminary steps in view of the general NVST objectives. In particular, the measurement procedure is a preliminary step for high precision polarimetry observation since we presently adopt a temporal and single-beam step-wise modulation. We have ignored the measurement error caused by atmospheric seeing and expect that the spatial smearing can be mitigated by implementing the adaptive optics (AO) technique. One high -order solar AO system has been developed (Rao et al. 2016). However it has not been combined with any existing terminals up to now. Combining the AO system with other terminals is our following instrumentation update.

In Section 2, we describe the main characteristics of the spectro-polarimetric observation system. In Section 3, we present our polarization modulation method and emphasize the importance of calibrating the instrument polarization for our polarimetry. Section 4 deals with the calibration method and procedure. We estimate the calibration accuracy and influence of the spectrograph position angle using the continuous calibration carried out in 2017 and 2019. Scientific observations for an active region are presented in Section 5 and applied to verify the calibration credibility and evaluate the real polarimetric sensitivity of our polarimetry.

2 SALIENT FEATURES OF THE SPECTRO-POLARIMETRIC OBSERVATION SYSTEM AT THE NVST

Figure 1 presents the optical system of the NVST polarimeter, mainly including a 98-cm aperture vacuum telescope on an alt-azimuth mount, a vertical multi-wavelength spectrograph and polarization modulator.

An ICU consisting of a linear polarizer and a $\lambda/4$ retarder is installed at the secondary focus (F2). As demonstrated in the upper-left corner of Figure 1, it is mounted in the front of a cylindrical device, which has a central hole in the radial axis and allows the light to go through along the optical axis for scientific observations. When we perform the calibration, the device rotates and its cylindrical axis is moved to the optical axis direction, which enables ICU to enter the optical path (Qin et al. 2018). The effective aperture of ICU is about 36 mm. We utilize a Wire Grid Versalight polarizer from Meadowlark Optics. This kind of polarizer offers the broadest and highest field of view and reflects another polarization state, which can decrease the effect of thermal expansion in the vacuum system. The retarder implemented is a zero-order achromatic waveplate consisting of quartz and MgF2 materials. It is manufactured by Union Optics. The thicknesses of quartz and MgF2 materials are 0.521 mm and 0.415 mm, respectively, which ensure the retardation variation is within $90^\circ \pm 10^\circ$ in a wide range of wavelengths from 520 nm to 1083 nm. Retardance measurements at several wavelengths of interest are given in Table 1. In order to improve the parallelism of the retarder, a double-separation structure is adopted, which makes the beam-deviation of each plate (quartz or MgF2) less than 1 arcsec. The reflectivity is less than 0.1% by coating anti-reflective films. Both the polarizer and retarder can be rotated independently relative to the reference axis (i.e., the axis of the polarizer at its home position), which is parallel to the telescope elevation and defines the direction of the Stokes $+Q$ in the analysis. Requirements on the accuracy of the polarization axis and the gear control of the stepper motor are about 0.5° and 0.002° respectively. Because there is no short pathway between ICU and the observation room, we have to remotely control ICU by using wireless technology.

Table 1 Retardance of the ICU Waveplate at Different Wavelengths

Wavelength (nm)	Retardance (degree)
525.0	90.72
532.4	91.74
617.3	98.54
854.2	92.81
864.8	92.08
1074.7	84.38
1083.0	85.04

In the Coudé laboratory setup as shown in the right of Figure 1, the main terminals are composed of a high resolution imaging system and a high dispersion spectrograph. They are arranged perpendicularly to each other. The entrance slit of the spectrograph is just set at the Coudé focus of the telescope (F3). It is noted that at present, both the AO system and two-dimensional (2D) field scanner (enclosed by a dashed box) have not been co-operated with the spectro-polarimetric observation and are ignored in the current work. Before the focus F3, we utilize a beam splitter (M_{45}) to distribute the incoming light into the imag-

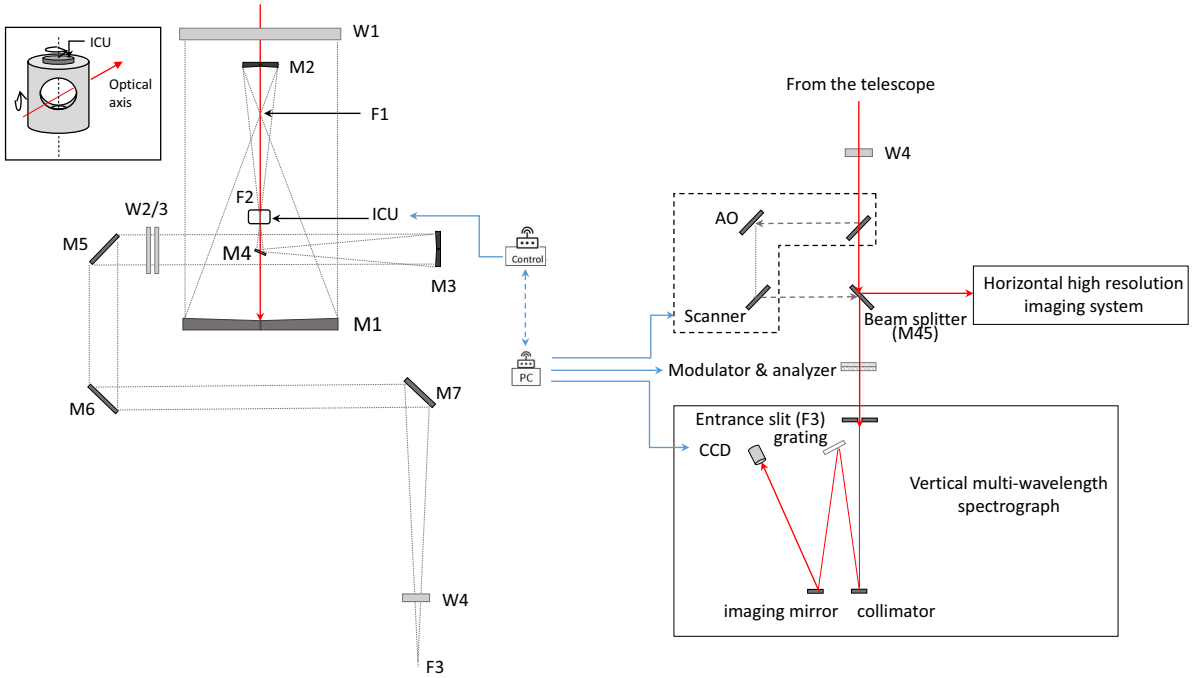

Fig. 1 Optical layout of the spectro-polarimetric observation system of the NVST. The telescope assembly is displayed on the left. The main optics implements an on-axis Gregorian design including the primary (M1) and secondary (M2) mirrors. M1 has a paraboloid figure and M2 has an ellipsoid one. After the secondary focus (F2), it is a Coudé train feeding the light beam down to the laboratory by utilizing a relay mirror (M3, ellipsoid figure) and four folding mirrors (M4, M5, M6 and M7). All optical elements are installed in two evacuated tubes, which are sealed by vacuum windows W1-2 and W3-4, respectively. An ICU is installed at the secondary focus (F2) and its mechanical device is demonstrated at the upper left corner. Backends in the laboratory are shown on the right. Both the AO system and field scanner enclosed by a *dashed box* are not included in the current optical path, which is indicated by *red lines*. See the text for more details on the spectrograph, the polarization modulator and analyzer. ICU is remotely controlled though a wireless technique by a PC in the observation room, which also controls the polarization modulator and cameras.

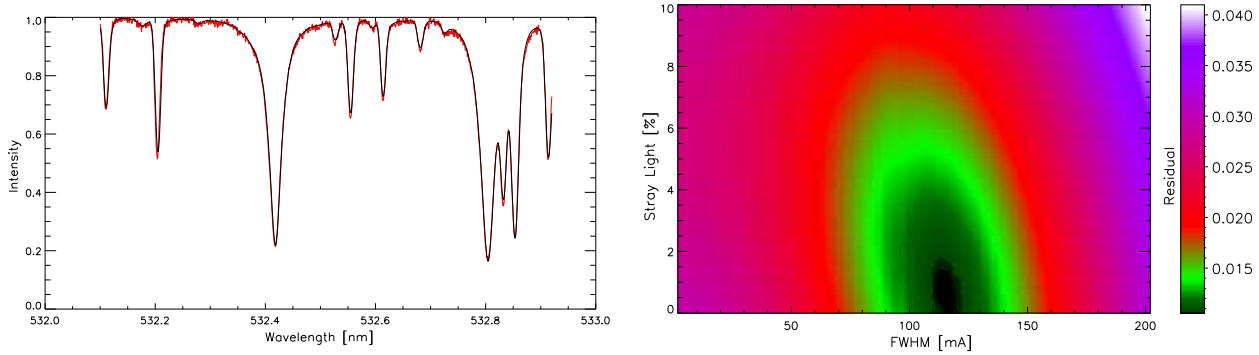

Fig. 2 Comparison of the observed spectral profile with the FTS atlas around Fe I 532.4 nm. *Left*: The FTS profile (the *black line*), modified by the instrumental profile and stray light, is superposed on the observed profile (the *red line*). *Right*: the residual χ^2, as defined in Eq. (1), between these two profiles with respect to the changes in the FWHM of the instrument profile and stray light.

ing system and spectrograph. In this situation, slit-jaw images can be reordered by using the imaging system. All the backends in the laboratory are relatively static, but they can be synchronously rotated as a whole in the azimuth orientation of the spectrograph in order to compensate the image rotation.

The multi-wavelength spectrograph can measure three spectral lines simultaneously, including two chromospheric lines (Hα and Ca II 854.2 nm) and one photospheric Fe I line at 532.4 nm. In order to concentrate on the spectro-polarimetric observation, M_{45} is specially designed to allow a wavelength band of 532.4 ± 5 nm to enter the spectrograph and reflect the other light into the imaging system monitoring the slit position. As a result, Hα and Ca II spectral observations are not available. Instead, high resolution imaging observations at some specific wavelengths (e.g., Hα, TiO-band or G-band) can be obtained simultaneously with spectro-polarimetric observation.

The Fe I 532.4 nm line is sensitive to the magnetic field with a Landér factor g of 1.5. It is also employed by the Solar Magnetism and Activity Telescope (SMAT) at Huairou Solar Observing Station (Ai & Hu 1986). A 1200 mm^{-1} grating is installed to get the Fe 532.4 nm line from the 2nd order onto the camera. The camera is a 14-bit PCO4K CCD with a full size of 4008×2672 pixels, and a pixel size is $9\mu\mathrm{m} \times 9\mu\mathrm{m}$. The saved data are 2-pixel binnings over columns and rows in order to increase the signal level. The wavelength sampling is of order 0.001 nm pixel^{-1} after binning and wavelength range is about 1.336 nm (i.e., $0.001 \times 2672/2 = 1.336$ nm). By comparison with the solar spectral atlases provided by the Fourier Transform Spectrometer (FTS) at the McMath-Pierce Solar Telescope, we can estimate the instrumental profile (a Gauss profile with a certain full width at half maximum, FWHM) and the stray light (α) by minimizing the χ^2 value, expressed as

$$\chi^2(\mathrm{FWHM}, \alpha) = \big[I_\lambda^{\mathrm{obs}} - (I_\lambda^{\mathrm{FTS}}(1-\alpha) \bigotimes G(\mathrm{FWHM}) + \alpha)\big]^2 . \quad (1)$$

Here the operator $\bigotimes$ represents the convolution and I_λ is a normalized profile to the continuum. One observed profile compared with the modified FTS profile is displayed in Figure 2. The minimum deviation between them can be obtained as the FWHM is equal to 118 mÅ and the α equal to 0.6%.

An assembly consisting of polarization modulator and analyzer is installed in front of the spectrograph slit. It is composed by a step-wise rotating retarder and a fixed linear polarizer. Both are manufactured by Huairou Solar Observing Station. Both the modulator and analyzer have effective apertures of 36 mm. The retardance of the modulator is optimized to be 127° at 532.4 nm to obtain equal modulation efficiency for different Stokes states. It is measured to be $127.8^\circ \pm 0.02^\circ$ in the laboratory. The angle between the fast axis of the modulator at the origin and the transmission axis of the analyzer is accurately measured to be $31.06^\circ \pm 0.06^\circ$ in the laboratory and taken into account in the demodulation process. Next, the transmission axis of the analyzer is placed parallel to the slit orientation. Inevitably, there may be an angular offset due to the installation error. Since it is not so easy to precisely measure this angle offset, we prefer to use a mechanical positioning to fix the assembly position with respect to the slit and ensure the reset accuracy. In addition, some interference fringes are apparently present in the spectral data. In order to efficiently eliminate the fringes, we tilt the assembly to make a small wedge angle between the glass surface and the slit surface.

3 SPECTRO-POLARIMETRIC OBSERVATION OF THE NVST

In the present NVST configuration, the polarization modulation is performed by step-wise rotations of the retarder and the intensity of only a single beam selected by the analyzer is measured. The modulated beam intensity (I_{obs}), as a function of four incoming Stokes parameters (S_{in}), the modulator rotation angle (θ) and its retardance (δ), is given by

$$\begin{aligned} I_{\mathrm{obs}}(\theta, \sigma) =& I_{\mathrm{in}} + Q_{\mathrm{in}}(\cos^2 2\theta + \sin^2 2\theta \cos\delta) \\ &+ U_{\mathrm{in}}[\sin 2\theta \cos 2\theta (1 - \cos\delta)] \\ &- V_{\mathrm{in}}(\sin 2\theta \sin\delta) , \end{aligned} \quad (2)$$

or expressed using matrices

$$I_{\mathrm{obs}} = M \cdot S_{\mathrm{in}} . \quad (3)$$

Here S_{in} means the incoming Stokes parameters *toward* the modulator. M represents the modulation process of the retarder. In order to derive the full Stokes parameters, the retarder is rotated to eight positions step-by-step with an interval of 22.5° in one-half rotation (i.e., $\theta = 0^\circ, 22.5^\circ, ..., 180^\circ$). The accuracy of the gear control for the stepper motor is 0.002°. The CCD takes images synchronously with the positioning of the retarder. To reach high polarization sensitivity we have to record n frames at each position. The camera does not record any images in the second half-rotation between 180° and 360°. As a result, we construct an 8×4 modulation matrix M and obtain an observed 8×1 intensity matrix I_{obs}, i.e., [I^1_{obs}, I^2_{obs}, ... I^8_{obs}]^T. Here I^i_{obs} corresponds to the spectral image integrated over n frames.

An appropriate demodulation (i.e., successive addition and subtraction of images) is then applied, which is represented by a demodulation matrix D. The process may be expressed as

$$\begin{aligned} D \cdot I_{\mathrm{obs}} &= D \cdot M \cdot S_{\mathrm{in}} \\ &= D \cdot M \cdot M_{M_{45}} \cdot M_T \cdot S_{\mathrm{sun}} , \\ S_{\mathrm{out}} &= X \cdot S_{\mathrm{sun}} . \end{aligned} \quad (4)$$

Here S_{sun} means the Stokes parameters generated by the Sun itself. S_{out} is the measured Stokes parameters demodulated from the observed intensities. M_T signifies the Mueller matrix of the telescope, followed by the Mueller matrix of the beam splitter, $M_{M_{45}}$, along the optical train. In other words, we have $S_{\mathrm{in}} = M_{M_{45}} \cdot M_T \cdot S_{\mathrm{sun}}$ in the case of scientific observation. We also can define a response matrix expressed as $X = D \cdot M \cdot M_{M_{45}} \cdot M_T$ and deduce the final expression in Equation (4). Only if X is precisely determined can the solar polarimetric signal S_{sun} be correctly retrieved. Here the process to determine X is

called the calibration of instrumental polarization. Being an alt-azimuth modified Gregorian telescope, the NVST has strong instrumental polarization, i.e., the response matrix seriously varies with the change of telescope pointing position during a day.

4 INSTRUMENTAL POLARIZATION CALIBRATION OF THE NVST

Based on Equation (4), we can use a constructed input Stokes vector to replace the unknown $S_{\rm sun}$ by taking advantage of ICU in order to derive the matrix X at a specific time. ICU can be moved into the vicinity of F2 if needed, which indicates that we cannot take into account the polarimetric properties of the first vacuum (W1), the primary mirror (M1) and the secondary mirror (M2), that are all located in front of ICU. Here we assume that their polarization effects are negligible since they are axi-symmetric about the optical axis.

4.1 Measurement of the Response Matrix X

Firstly, we make the telescope point to the quiet region around the solar disk center assuming the incoming light is taken as unpolarized (Stenflo 2005). Meanwhile, the spectrograph, together with the M_{45}, the polarization modulator and analyzer, is fixed at the initial position ($\theta_{\rm sp} = 0$) during the calibration process, despite rotation of the solar image. Influence of the spectrograph azimuth angle will be discussed in detail in Section 4.3.

Secondly, ICU successively generates six kinds of polarized light by rotating its polarizer and retarder independently. The six pairs of rotation angles (θ_p, θ_r) are [0°, 0°], [45°, 45°], [90°, 90°], [135°, 90°], [135°, 135°] and [135°, 180°], respectively. Thus the constructed input Stokes vector is given by

$$S^c_{\rm in} = M_r(\theta_r) \cdot M_p(\theta_p) \cdot [1, 0, 0, 0]^T , \qquad (5)$$

where M_p and M_r represent the Mueller matrices of the polarizer and retarder in ICU, respectively. The $S^c_{\rm in}$ of the six cases actually make up a 4×6 matrix.

To measure each kind of input Stokes vector, we perform an eight-step modulated spectro-polarimetric observation as described above. At each modulation step we intend to take five frames continuously. Meanwhile, more pixel binning and shorter exposure time are adopted to record a single frame. After adding five frames taken in one modulation state, we further integrate the continuum spectrum both in the wavelength direction (about 0.1 nm) and the spatial direction (about 1/5 of the slit length) to get the observed intensity value $I^c_{\rm obs}$, which is a wavelength- and spatially-independent value. As a result, an 8×6 matrix is composed by the measured intensities, and it can be converted to a 4×6 matrix after demodulation (i.e., $S_{\rm out}$). We depict both the constructed $S^c_{\rm in}$ and measured (or demodulated) $S_{\rm out}$ in Figure 3.

Eventually, the response matrix X can be derived from the following equation by matrix inversion

$$S_{\rm out} = X \cdot S^c_{\rm in} . \qquad (6)$$

It totally takes about 53 s to finish one complete calibration measurement, which indicates that we assume the polarization property of the polarimeter is stable during this period.

4.2 Calibration Accuracy

The calibration accuracy strongly depends on our knowledge about the $S^c_{\rm in}$, or particularly speaking, the polarization properties of the optical elements of ICU. Therefore in addition to the 16 elements of the response matrix X, two more free parameters related to ICU are taken into account as we construct the $S^c_{\rm in}$.

- The retardance of the ICU retarder (δ^c_r). The value tested in the laboratory is regarded as an initial value.
- An offset angle ($\theta^c_{\rm off}$) between the ICU polarizer and the retarder axis accounts for the misalignment during installation.

A change of δ^c_r and $\theta^c_{\rm off}$ only affects the input vectors $S^c_{\rm in}$. All these 18 free parameters can be instantly calculated by minimizing the residual with respect to these two parameters by a gradient method (Beck et al. 2005), as expressed by

$$\chi^2_i(\delta^c_r, \theta^c_{\rm off}) = \sum_{i=0...3} (X \cdot S^c_{\rm in}(\delta^c_r, \theta^c_{\rm off}) - S_{\rm out})^2_i . \qquad (7)$$

$S_{\rm out}$ is the directly measured output vectors, and the term ($X \cdot S^c_{\rm in}$) can be regarded as the predicated output. Once χ^2 reaches the minimum, the solutions of δ^c_r and $\theta^c_{\rm off}$ are determined. The X is finally obtained.

In Figure 3, it is clearly seen that the directly measured vector $S_{\rm out}$ deviates far from the input Stokes vector $S^c_{\rm in}$, but manifests a good agreement with the predicated output vector. It means that we can reproduce the output vector from $S^c_{\rm in}$ well with the correct response matrix X. In other words, we can retrieve the $S^c_{\rm in}$ from the observed vector as long as the response matrix X is correctly determined. The largest deviation is present in Stokes I, which is consistent with reports from other authors (Beck et al. 2005). Consequently, we estimate the calibration accuracy from the deviation, i.e., the residual value between the measured and final predicated $S_{\rm out}$, expressed as $\sum_n |X \cdot S^c_{\rm in} - S_{\rm out}|$ ($n = 0...5$) for each Stokes vector.

In order to investigate the time evolution of the response matrix X during a day and the calibration accuracy

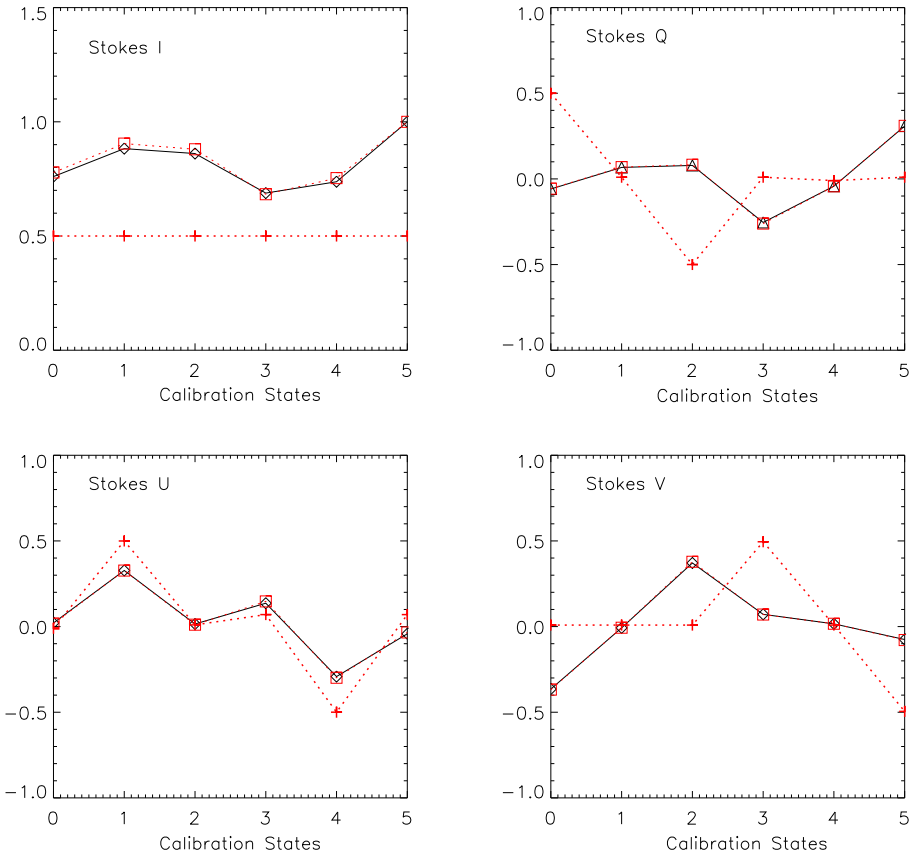

Fig. 3 Stokes vectors (I, Q, U, V) of a calibration measurement. *Red dotted with crosses*: $S^c_{\rm in}$, the constructed input Stokes vectors of six cases, which are calculated by a given retardance and six pairs of rotation angles of ICU. *Black solid with diamonds*: $S_{\rm out}$, the measured Stokes vectors, which are demodulated from the observed intensities. *Red dotted with squares*: the predicated output vectors, i.e., the term $X \cdot S^c_{\rm in}$.

and stability, we carried out several times of one-day continuous calibrations in 2017 and 2019. (We are reminded that the spectrograph was not available in 2018.)

In Figure 4, we show a typical response matrix measured from a 7-hour continuous calibration. It actually comprises the measurement on 2017 February 15 and 16. There is no apparent discontinuity between these two successive days and all the matrix elements smoothly change with time. Elements in the first column of the matrix, which indicate the cross-talk from I to I, Q, U and V, respectively, are more diffuse at first glance, but their variations are actually one-magnitude lower than others.

In Figure 5, we present the time evolution of the residual value between the measured and predicated output vectors (Stokes Q, U and V) during this period. The averaged residual is about 3×10^{-3} and the standard deviation is about 1.3×10^{-3}. In detail, from the results of the whole day, it is seen that the residuals of Stokes Q and U are larger than those of Stokes V, particularly after hour angle of -1^h. The largest residual ($\sim 6.6 \times 10^{-3}$) is found in Stokes U at hour angle of about 2^h. In addition, the Stokes Q residuals after -1^h even exhibit a fluctuation in a sinusoidal distribution, while those of Stokes U manifest a negative sinusoidal distribution. It is implied that they are closely related.

As we mentioned above, the retardance of the ICU retarder (δ^c_r) is considered to be a free parameter during the calculation. It is further revealed that this retardance regularly changes during the continuous calibration and exhibit a correlation with the variation of the Stokes I intensity obtained by the demodulation. As displayed in Figure 6, the intensity of Stokes I shows an increase-stable-decrease trend from hour angle of -4^h to 3^h, which is closely related to the change of solar elevation angle. During this period, δ^c_r gradually increases from 92° to 98° and then becomes stable around the culmination time, but there is no obvious decrease since then. It is worth noting that the retardance after hour angle of -1^h manifests a larger diffusion range than before.

In contrast, another free parameter, the offset angle ($\theta^c_{\rm off}$), has a steady value of around 0.35 degree. Since this value is fairly stable not only on February 15th and 16th but also on other days, we eventually fix it and take into account the remaining 17 parameters.

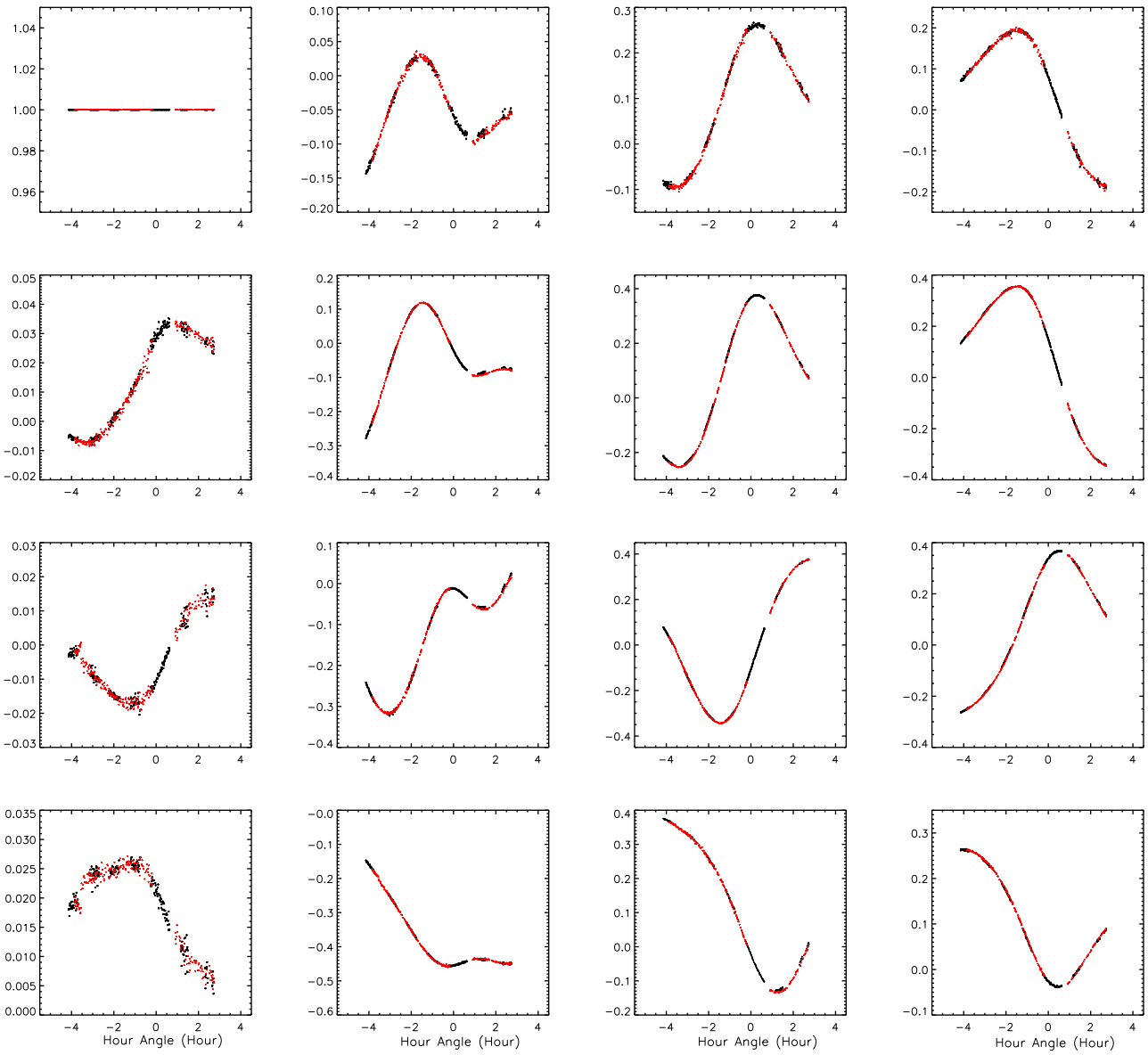

Fig. 4 Response matrix X of NVST as function of hour angle of the Sun in about 7 hours. It consists of the measurements on 2017 February 15 (*black dots*) and 16 (*red dots*).

4.3 Influence of Spectrograph Azimuth Angle

To compensate the image rotation on the focal plane, the spectrograph, together with the beam splitter (M_{45}), polarization modulator and analyzer, needs to be synchronously rotated in the azimuth orientation ($\theta_{\rm sp}$) during scientific observations. Since the Mueller matrix characterizes not only the optical properties but also the orientation of each element in the optical path, the response matrix $X(\theta_{\rm sp}=0)$ precisely measured at the original azimuth angle needs to be transformed to $X(\theta_{\rm sp}=\theta)$ by coordinate rotation in order to calibrate scientific observations carried out with the azimuth angle of θ.

In the case of azimuth angle θ, Equation (4) describing the modulation process can be modified to be

$$D\cdot I_{\rm obs} = D\cdot M\cdot M_{M_{45}}\cdot Rot(\theta)\cdot M_T\cdot S_{\rm sun}, \qquad (8)$$

in which we define

$$X(\theta_{\rm sp}=\theta) = D\cdot M\cdot M_{M_{45}}\cdot Rot(\theta)\cdot M_T \qquad (9)$$

with the matrix of coordinate rotation

$$Rot(\theta) = \begin{bmatrix} 1 & 0 & 0 & 0 \\ 0 & \cos 2\theta & \sin 2\theta & 0 \\ 0 & -\sin 2\theta & \cos 2\theta & 0 \\ 0 & 0 & 0 & 1 \end{bmatrix}. \qquad (10)$$

To realize the transformation from $X(\theta_{\rm sp}=0)$ to $X(\theta_{\rm sp}=\theta)$ according to Equation (4) and Equation (9), it

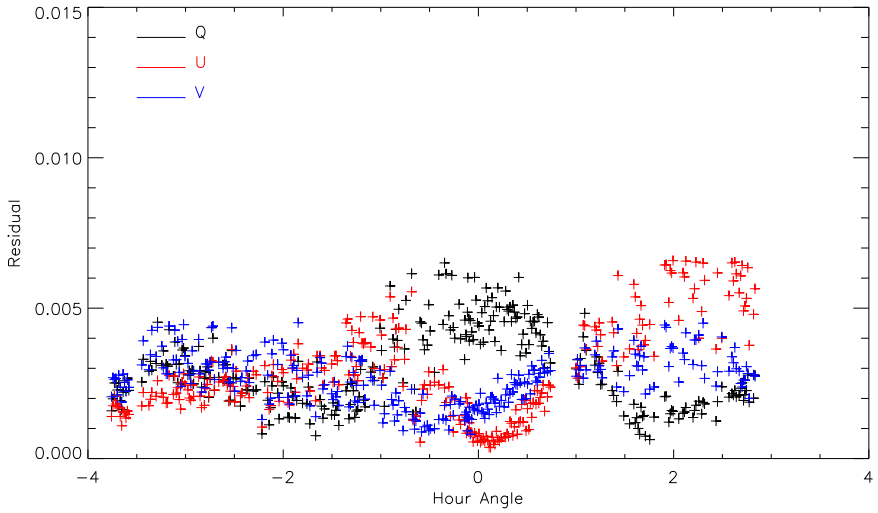

Fig. 5 Time evolutions of the residuals between the measured and calculated Stokes vectors using the correct response matrix X. Stokes Q is depicted in *black*, U in *red* and V in *blue*. The observational data are the same as what are displayed in Fig. 4.

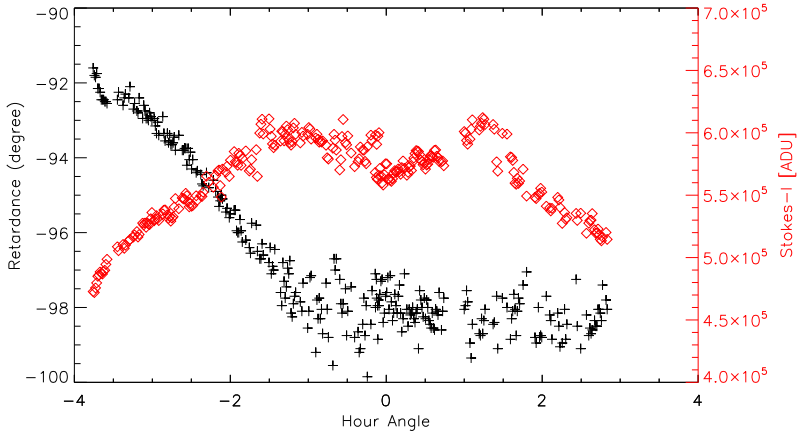

Fig. 6 Change of the retardance of the ICU retarder during a one-day continuous calibration (*black crosses*) superposed on variation of the Stokes I after the demodulation (*red diamonds*).

is obliged to have a good knowledge of the modulation matrix M and the Mueller matrix of the beam splitter $M_{M_{45}}$. To know the matrix M, as mentioned in Section 2, both the retardance of the modulator and the gear control precision of the modulator rotation are precisely measured in the laboratory. To know the matrix $M_{M_{45}}$, we firstly test it in the laboratory using the Mueller Matrix Measurement System, which is sensitive to 10^{-3} for each matrix element for weak polarization optical elements. The general principle of such measurement can be found in Ichimoto et al. (2006). We also compare the $M_{M_{45}}$ with the result measured by applying the NVST polarization observation system (Peng et al. 2018). A typical result of the $M_{M_{45}}$ is

$$M_{M_{45}} = \begin{bmatrix} 1.0000 & 0.0232 & 0.0007 & 0.0004 \\ 0.0227 & 1.0003 & 0.0023 & --0.0115 \\ --0.0004 & 0.0025 & 0.9006 & 0.4328 \\ 0.0008 & 0.0113 & --0.4360 & 0.8999 \end{bmatrix}. \quad (11)$$

One experiment involving the transformation was carried out on 2019 February 12 as shown in Figure 7. We directly measure X at the azimuth angle of $0°$ and $30°$, respectively, at different times. It is clearly seen that the response matrix dramatically changes in time due to the change of the azimuth angle. However as long as the parameters mentioned above are accurately given, the transformation from $X(\theta_{\rm sp} = 30°)$ to $X(\theta_{\rm sp} = 0°)$ can be correctly accomplished, i.e., the response matrix recovers good continuity in time after transformation. In return, it is indicated that the measurement of Mueller matrices of optical elements and the response matrix itself is fairly precise.

5 APPLICATION TO OBSERVATIONS

A δ-class sunspot region (NOAA Active Region (AR) 12645, S10 W60) was observed in Fe I 532.4 nm using the NVST polarimeter on 2017 April 5. The slit width is

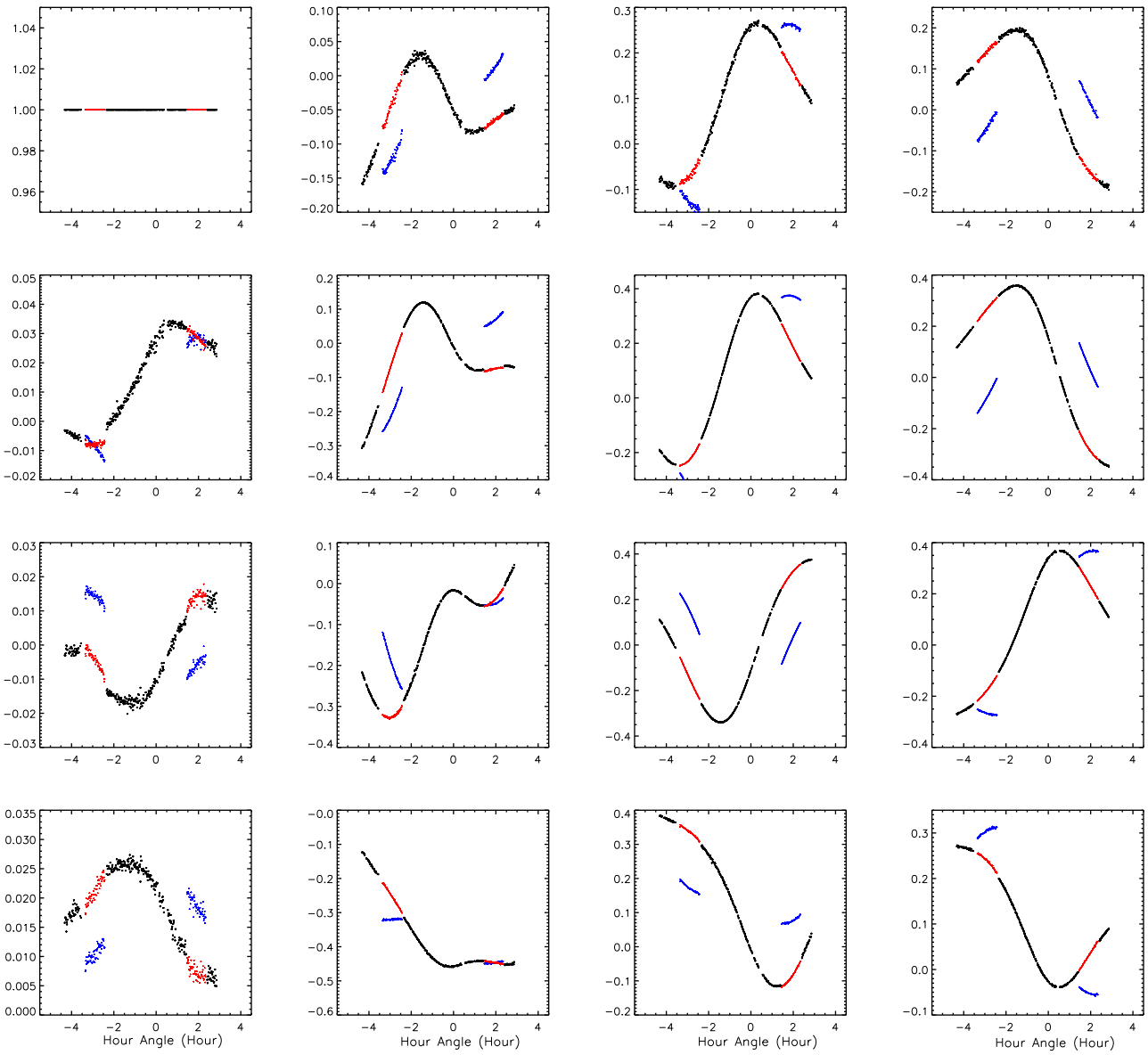

Fig. 7 Response matrix X of NVST as a function of hour angle of the Sun on 2019 February 12. *Black dots*: the response matrix measured with the azimuth angle of the spectrograph of $0°$, i.e., $X(\theta_{\rm sp} = 0°)$. *Blue dots*: the response matrix measured with the azimuth angle of $30°$, $X(\theta_{\rm sp} = 30°)$. *Red dots*: the transformed response matrix from $\theta_{\rm sp} = 30°$ to $\theta_{\rm sp} = 0°$.

0.1 mm corresponding to 0.45 arcsec on the solar image. Spatial sampling along the list is 0.082 arcsec pixel^{-1} and the field-of-view is about 137 arcsec, limited by the slit length.

We perform an 8-step polarization modulation and collect 20 frames at each modulation state. The exposure time of a single image is 30 ms, and by collecting all frames at each modulation state, the typical noise level reaches $10^{-3}I_c$. As a result, it totally takes about 23 s to complete the modulation at one slit position. The azimuth angle of the spectrograph position is set at $\theta_{\rm sp} = 0$ in both the calibration measurement and the scientific observation time, which happens to make the slit almost parallel to the solar radial orientation, going through the major sunspot and other satellite sunspots. Calibration measurements of the instrumental polarization are carried out both before and after the scientific observation. The time interval of these two calibrations is less than 30 minutes, but the response matrix apparently and linearly changes during this period. Therefore, we linearly interpolate the response matrix for the time of the scientific observation in order to calibrate the instrumental polarization at that time.

Before demodulating the observed $I_{\rm obs}$, we applied the standard spectral data reduction routines, including dark current subtraction and flat-fielding.

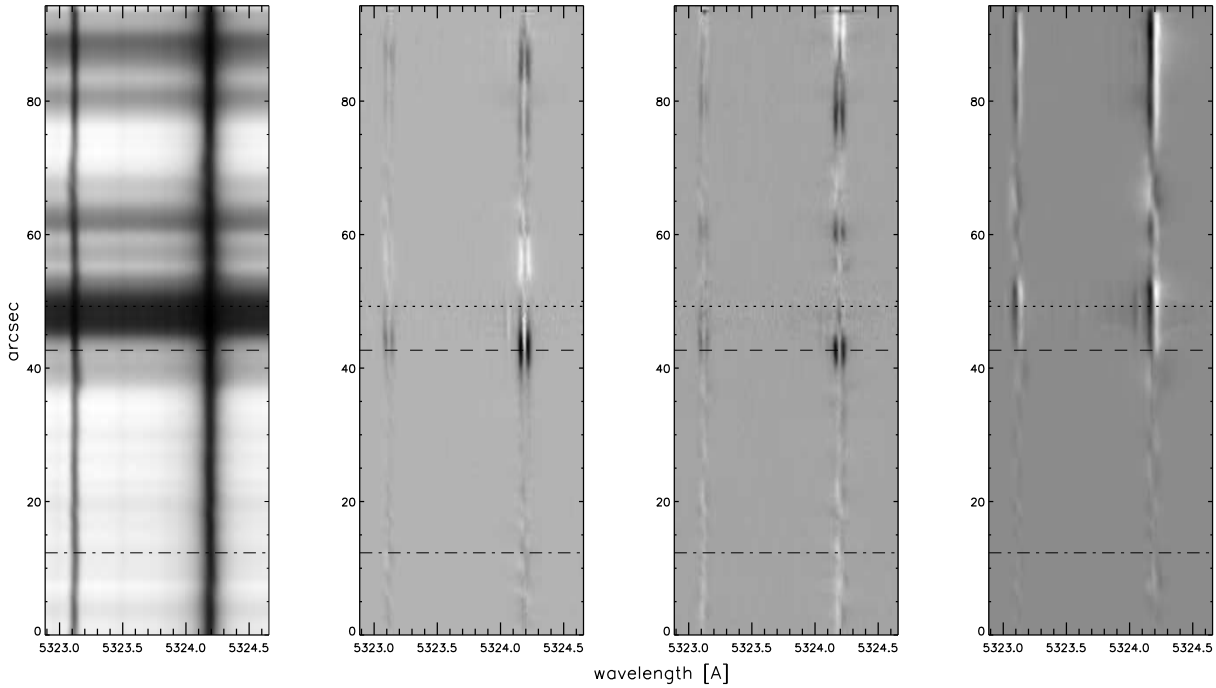

Fig. 8 2D Stokes spectra along one slit in NOAA AR 12645. *Left to right*: I, Q/I, U/I and V/I. The *dotted-*, *dashed-* and *dot-dashed-lines* indicate the typical sunspot umbra, penumbra and quiet sun areas, respectively, whose one-dimensional Stokes profiles are plotted in Fig. 8 from top to bottom.

The Stokes vectors $S_\lambda^{\rm sun}$ are derived after calibrating instrumental polarization. However, some residual cross-talk still exists between different Stokes vectors even after the calibration. The relationship to the real Stokes vectors from the Sun, $S_\lambda^{\rm real}$, can be expressed as the following Equation (12) with an assumption that the most serious cross-talk comes from Stokes I

$$\begin{aligned} S_\lambda^{\rm sun} &= S_\lambda^{\rm real} + a_{I\rightarrow S} I_\lambda \,, \\ \frac{S_\lambda^{\rm sun}}{I_\lambda} &= \frac{S_\lambda^{\rm real}}{I_\lambda} + a_{I\rightarrow S} \,. \end{aligned} \tag{12}$$

Here, $a_{I\rightarrow S}$ means the proportion of the cross-talk coming from the Stokes I and it is wavelength- and spatially-independent. If we take an expression of S_λ/I_λ, we can easily estimate this cross-talk in the continuum wavelength from the 2D Stokes image, since the local polarization signal $S^{\rm real}$ is supposed to be zero. From the observation of NOAA AR 12645, we estimate that the $a_{I\rightarrow q}$, $a_{I\rightarrow u}$ and $a_{I\rightarrow v}$ are 6.5×10^{-3}, 1.2×10^{-3} and 5.5×10^{-3}, respectively. The averaged value is about 4×10^{-3}.

After this estimation, we force the polarization signal at the continuum to be zero and show the resulting 2D Stokes images in Figure 8. Spatial changes along the slit are clearly exhibited in full Stokes profiles. A large scale Evershed flow around the main sunspot is clearly revealed in Stokes I, which is demonstrated as an obvious tilt along the slit direction of the spectrum inside the sunspot. Based on the Doppler shift calculation, it is found that the line-of-sight speed varies from around $1\,{\rm km\,s^{-1}}$ at the border between the umbra and the penumbra to a maximum of $1.8\,{\rm km\,s^{-1}}$ in the middle of the penumbra and falls off to zero at the edge of the penumbra. In addition, typical symmetric or anti-symmetric Stokes Q, U and V profiles are present around the sunspot. The full Stokes profiles taken from the umbra, penumbra and quiet region are displayed in Figure 9. From these observed results, we can estimate the polarimetric sensitivity, i.e., the standard deviation of the noise level in the continuum. In Figure 9, the noise level in Stokes V/I is about 2.1×10^{-3} and the results of Stokes Q/I and U/I are very close to it. In fact, the noise level is closely related to the total integration time (i.e., the number of integrated frames taken at one modulation state). Some investigations with different integration times are listed in Table 2. The noise level increases as the integration time decreases, and it reaches 3.3×10^{-3} in 14 s and 5.2×10^{-3} in 10 s.

Table 2 Noise Level in Continuum with Different Integration Times

Integration time (s)	23	14	10
Integrated Frame number (n)	20	10	5
Noise level	2.1×10^{-3}	3.3×10^{-3}	5.2×10^{-3}

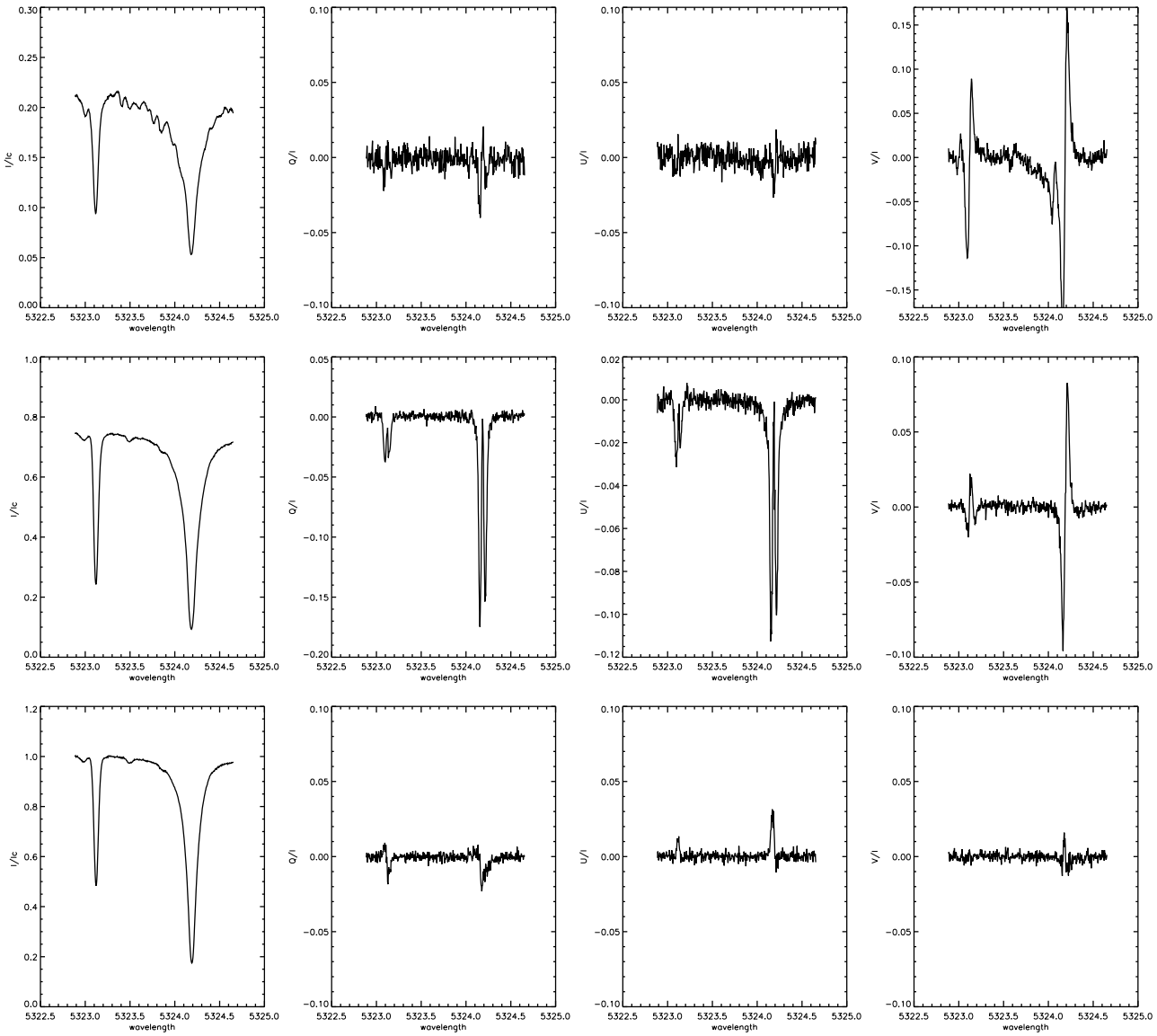

Fig. 9 Stokes profiles observed in NOAA AR 12645. *Left to right*: I/I_c, Q/I, U/I and V/I. I_c is the continuum intensity of the quiet Sun profile. *Top to bottom*: Stokes profiles taken from the sunspot umbra, penumbra and quiet Sun, respectively, as marked by different lines in Fig. 8.

6 DISCUSSION AND SUMMARY

Spectro-polarimetric observation is the third phase of the NVST multi-wavelength spectrograph operation. Initially, spectrograph installation and its salient function were accomplished in 2013 (Wang et al. 2013). These were followed by the precise data reduction and 2D field scan (Cai et al. 2018). The efforts presented in this paper are to develop the capability of spectro-polarimetric observation for future vector magnetic field measurements. As mentioned above, these efforts are only the preliminary steps in view of the high precision polarimetry observation, particularly, taking into account the slow modulation rate, the 2D spatial scan, the combination with the AO system, etc.

In this work, we mainly deal with important topics of the polarimetric calibration of the instrument. The response matrix of the NVST can be accurately determined by utilizing ICU. It is verified that both the facilities and measurement procedures are fairly stable and credible, as demonstrated by the comparison between the calibration results on 2017 February 16 (Fig. 4) and on 2019 February 12 (Fig. 7). The time variation of each matrix element indicates almost the same morphology and magnitude, which suggest that the 2-year gap has no obvious effect on the daily evolution of the response matrix from the dates of the 12th to 16th.

The calibration accuracy can reach up to $3\pm1.3\times10^{-3}$ considering that the retardance of the ICU retarder (δ_r^c) is a

free variable. Variation of the retardance and the intensity of Stokes I after the demodulation show a good correlation during the continuous calibration. The straightforward reason is not clear, but the temperature increase, during the continuous observation at the secondary focus where ICU is located, may be a candidate to explain this feature. More detection and experiments are needed to confirm it. In addition, from the comparison of Figure 5 with Figure 6, we find that the large fluctuation of the calibration residual is present when this retardance is calculated with a relatively large scatter, which indicates that the main contribution to the calibration errors comes from the imprecise measurement of this retardance.

Based on the spectro-polarimetric observation for NOAA AR 12645, it is verified that, firstly, the calibration result is credible and the instrumental polarization is largely removed. Secondly, after calibrating the instrumental polarization, the residual cross-talk from Stokes I to Stokes Q, U and V is about 4×10^{-3} on average, which is consistent with the calibration accuracy and close to the photon noise (or statistical noise). However, we do not investigate the residual cross-talk among Stokes Q, U and V for the time being. We intend to perform a statistical analysis for the amount of Stokes profiles taken from isolated α-class sunspots when they are approaching the disk center and investigate the correlation among the Stokes profile shapes (Kuhn et al. 1994). Thirdly, it is revealed that an integration time over 20 s is needed for the present system in order to archive a polarimetric sensitivity or a detection limit of 10^{-3}. A slow rate of modulation is indeed an issue for our present system and a continuous modulation process is now under consideration.

As mentioned in the caption of Figure 1, both the field scanner and AO system have not been included into the present optical system yet. Up to now, we have carried out the Mueller matrix measurement for each element independently in the laboratory. We will integrate these two elements in the upcoming instrument update.

An IDL-based software package has been developed for the spectral data reduction and polarimetric calibration. Furthermore, we have accomplished the full Stokes inversion using the Helix code (Lagg et al. 2004), which is based on the Unno-Rachkowsky analytic solution of the radiative transfer for polarized radiation in a Milne-Eddington atmosphere approximation. The vector magnetic field and other physical quantities are retrieved. However considering the main issue of this paper, we do not provide the inversion results in this paper.

Acknowledgements This work was supported by the National Natural Science Foundation of China (Grant Nos. 11873091, 11773040, 11773072 and 11373044). We are grateful to the anonymous reference for his thoughtful discussion and help clarifying this manuscript.

References

Ai, G. X., & Hu, Y. F. 1986, Acta Astronomica Sinica, 27, 173
Anan, T., Ichimoto, K., Oi, A., et al. 2012, Proceeding of the SPIE, 8446, 84461C
Anan, T., Huang, Y.-W., Nakatani, Y., et al. 2018, PASJ, 70, 102
Baur, T. G., House, L. L., & Hull, H. K. 1980, Sol. Phys., 65, 111
Beck, C., Schmidt, W., Kentischer, T., & Elmore, D. 2005, A&A, 437, 1159
Cai, Y.-F., Xu, Z., Chen, Y.-C., et al. 2018, RAA (Research in Astronomy and Astrophysics), 18, 042
del Toro Iniesta, J. C. 2003, Introduction to Spectropolarimetry (Cambridge : Cambridge Univ. Press), 244
Harvey, J., Livingston, W., & Slaughter, C. 1972, in Line Formation in the Presence of Magnetic Fields, 227
Hofmann, A., Arlt, K., Balthasar, H., et al. 2012, Astronomische Nachrichten, 333, 854
Hou, J.-F., Wang, D.-G., Deng, Y.-Y., Sun, Y.-Z., & Zhang, Z.-Y. 2017, Chinese Physics B, 26, 089501
Ichimoto, K., Shinoda, K., Yamamoto, T., & Kiyohara, J. 2006, Publications of the National Astronomical Observatory of Japan, 9, 11
Ichimoto, K., Lites, B., Elmore, D., et al. 2008, Sol. Phys., 249, 233
Kiyohara, J., Ueno, S., Kitai, R., et al. 2004, Society of Photo-Optical Instrumentation Engineers (SPIE) Conference Series, 5492, Calibration of the Instrumental Polarization of the Domeless Solar Telescope at the Hida Observatory, eds. A. F. M. Moorwood, & M. Iye, 1778
Kuhn, J. R., Balasubramaniam, K. S., Kopp, G., et al. 1994, Sol. Phys., 153, 143
Lagg, A., Woch, J., Krupp, N., & Solanki, S. K. 2004, A&A, 414, 1109
Liu, Z., Xu, J., Gu, B.-Z., et al. 2014, RAA (Research in Astronomy and Astrophysics), 14, 705
Peng, J., Yuan, S., Jin, Z., Observatories, Y., et al. 2018, Astronomical Research & Technology, 15, 95
Qin, Y., Peng, J., Zhang, T., et al. 2018, Astronomical Research & Technology, 15, 315
Rao, C., Zhu, L., Rao, X., et al. 2016, ApJ, 833, 210
Skumanich, A., & Lites, B. W. 1987, ApJ, 322, 473
Skumanich, A., Lites, B. W., Martínez Pillet, V., & Seagraves, P. 1997, ApJS, 110, 357
Stenflo, J. O. 2005, A&A, 429, 713
Wang, R., Xu, Z., Jin, Z.-Y., et al. 2013, RAA (Research in Astronomy and Astrophysics), 13, 1240
Xu, Z., Jin, Z. Y., Xu, F. Y., & Liu, Z. 2014, in IAU Symposium, 300, Nature of Prominences and their Role in Space Weather, eds. B. Schmieder, J.-M. Malherbe, & S. T. Wu, 117